

Concurrent design for structures and material microstructures under hybrid uncertainties



Yongfeng Zheng^a, Yingjun Wang^a, Zhen Luo^b, Xiang Lu^{c,*}, Jinping Qu^{a,c,*}

^aNational Engineering Research Center of Novel Equipment for Polymer Processing, Key Laboratory of Polymer Processing Engineering (South China University of Technology), Ministry of Education, Guangdong Provincial Key Laboratory of Technique and Equipment for Macromolecular Advanced Manufacturing, School of Mechanical and Automotive Engineering, South China University of Technology, Guangzhou 510641, China

^bSchool of Mechanical and Mechatronic Engineering, University of Technology Sydney, NSW 2007, Australia

^cSchool of Chemistry and Chemical Engineering, Huazhong University of Science & Technology, Wuhan 430074, China

ARTICLE INFO

Article history:

Received 16 February 2021

Revised 23 March 2021

Accepted 10 April 2021

Available online 17 April 2021

Keywords:

Concurrent design

Material microstructures

Hybrid uncertainties

Smooth boundary

ABSTRACT

This study presents a novel topology optimization method for the robust design of structures and material microstructures. Uncertainties are usually ubiquitous and of different sources, and especially hybrid uncertainties widely exist in structural designs including external loads and material properties. Firstly, an orthogonal decomposition and uniform sampling (ODUS) method will be proposed to avoid the time-consuming double loops, in terms of load uncertainties described by upper and lower bounds. Secondly, a non-intrusive polynomial chaos expansion (NIPCE) is implicitly implemented, in terms of base material uncertainties subjected to Gaussian distributions. In the optimization formulation, the robust objective function is defined according to both the expectation and standard variation of structural compliance, and the sensitivity information with respect to the two-scale design variables are given in detail. Finally, an effective evolutionary method is employed to iteratively find the optimal topologies of the design. In addition, this study also defines a dimensionless index to evaluate the robustness of deterministic and robust designs. Three numerical examples are provided to demonstrate the efficiency of the proposed method, and 3D design results are fabricated by using appropriate additive manufacturing techniques.

© 2021 The Author(s). Published by Elsevier Ltd. This is an open access article under the CC BY-NC-ND license (<http://creativecommons.org/licenses/by-nc-nd/4.0/>).

1. Introduction

Topology optimization has been a popular numerical approach and applied to design various structures and material microstructures, to achieved specified properties and performance, e.g., [1–6,45]. So far, several types of topology optimization methods have been developed [7–13]. In particular, the bi-directional evolutionary topology optimization (BETO) method [14] shows many advantages in practical engineering practice, such as conceptual simplicity and implementation easiness. However, most existing studies pertaining to multi-scale topological designs are limited to deterministic assumption with no consideration for parameters variations in the design [15–20]. It is noted that uncertainties such as load disturbance, material imperfection, geometric and modelling errors, and manufacturing tolerance are ubiquitous in engineering practice. Conventional deterministic assumption may

result in design only meaningful in theory but not feasible in practice [21–24]. Amongst a range of uncertainties, load and material uncertainties are the most common ones. In most situations, it is hard to have complete information to describe accurate probability distribution functions related to load uncertainties by numerical simulations and experiments, such as shocks, vibrations, noises, and partial loads. Thus, non-probabilistic modelling approaches only requiring upper and lower bound information can be used to describe them [25,47]. Base material parameters such as elastic modulus and Poisson's ratio rarely exhibit perfect homogeneity due to a range of factors. For instance, in traditional manufacturing, material uncertainties can be induced by acidity variations during steel plate preparation, time, and temperature instability during heat processing, and different rolling procedures. In additive manufacturing, material uncertainties are also widespread during the melting and cooling process [26]. However, the uncertainties of the base material properties related to elastic modulus and Poisson's ratio have been well studied and complete information are available for describing their probability distributions. Hence, in this paper,

* Corresponding authors at: School of Mechanical and Automotive Engineering, South China University of Technology, Guangzhou 510641, China (J.P. Qu).

E-mail addresses: luxiang@hust.edu.cn (X. Lu), jqu@scut.edu.cn (J. Qu).

the Gaussian distributions will be directly adopted to characterize these uncertainties, according to the engineering experiences.

Topology optimization methods considering uncertainties can be roughly categorized as reliability-based topology optimization (RBTO) and robust topology optimization (RTO) [27–29]. When uncertainty information are easily obtained by experiments, simulations and experiences, constraints can be defined in RBTO models to satisfy the lowest failure probabilities [30,31], while RTO is a complementary to make structures insensitive to uncertainty factors [32,33]. Guo et al [34] established a confidence robust optimization formulation for structures and materials, where the unknown-but-bounded load uncertainties are considered. Wang et al. [35] investigated multi-scale non-probabilistic optimization problem, conducting the RBTO at macro and reliability-based design optimization at micro. Zheng et al [21] studied the concurrent design problem of dynamic structures, a hybrid dimensional reduction model is proposed to estimate the interval mean and variance of dynamic performance. He et al [36] proposed an improved hybrid perturbation analysis method to evaluate the robust objective function related to imprecise uncertainties, where various excitation frequencies are analyzed. Although there have been some research works related to the multi-scale RTO problems, they are associated with drawbacks. For instance, some studies only consider single uncertainty, so the design results may fail to satisfy the expected performance when suffering multiple uncertainties. Some methods involving nested double-loop computation in evaluating robustness have low efficiencies, which makes them difficult to solve relatively large-scale engineering problems. Hybrid uncertainties have been considered in the topology optimization design problems [36], but how much influence of load and material uncertainties on the concurrent designs still remains unknown.

To address the abovementioned drawbacks, this study performs concurrent design of structures and material microstructures, by considering both the load and material uncertainties. In terms of uncertainties (or variations) of the externally applied loads featured with unknown-but-bounded variables [27], an orthogonal decomposition and uniform sampling (ODUS) method is proposed to quantify them. Orthogonal decomposition can separate the uncertainty variables into several coefficients unrelated to finite element analysis to save the computational costs. By using uniform sampling, the original uncertainty problem is transformed into an augmented deterministic one with multiple cases, and then explicit sensitivities can be obtained to avoid the conventional double-loop procedure [37]. In terms of material uncertainties subjected to Gaussian distributions, a non-intrusive polynomial chaos expansion (NIPCE) is introduced to quantify the elastic modulus and Poisson's ratio uncertainties. The objective function is formulated to minimize the structural compliance subjected to two-scale volume constraints. Additionally, an efficient BETO method is employed to find the final topologies of structures and material microstructures, the macroscopic equivalent properties of material microstructures are evaluated by using the homogenization method. A dimensionless index is also defined to evaluate the robustness of deterministic and robust designs. Three numerical examples are provided to illustrate the effectiveness of the proposed method, 3D design results are fabricated by the additive manufacturing.

2. Problem statement and homogenization theory

2.1. Deterministic topology optimization formulation

For simplicity but without losing any generality, this paper investigates the concurrent design of structure periodically fas-

ioned by one type of identical microstructures. Based on the BETO method, the problem to minimize the mean compliance subjected to volume constraints can be defined as

$$\begin{aligned}
 & \text{Find : } \rho = [\rho_m, \rho_n]^T \quad (m = 1, 2, \dots, M; n = 1, 2, \dots, N) \\
 & \text{Minimize : } C(\rho) = U^T K U \\
 & \text{Subject to : } F^{(MA)} = K(\rho) U^{(MA)} \\
 & V^{MA*} - \sum_{a=1}^S V_a v_a(\rho_m) = 0 \\
 & V^{MI*} - \sum_{b=1}^T V_b v_b(\rho_n) = 0 \\
 & \rho_m, \rho_n = 0 \text{ or } 1
 \end{aligned} \tag{1}$$

where ρ is the interpolation points to be solved, ρ_m and ρ_n denote the design variables at macro and micro level, respectively. M and N are the total number of interpolation points at both macro and micro scale, respectively. C is the structural compliance, U is the structural displacement, K is the macroscopic stiffness matrix, and F is external force applied at the macrostructure. S and T are the total number of elements discretized at two scales. V^{MA*} and V^{MI*} are the defined material usages. V_a and V_b are the a -th and b -th elemental volume at the macro and micro scale, respectively, v_a and v_b are the changing volumes related to a -th and b -th elements. It is noted that V_a and V_b are constant values when mesh sizes are given, v_a and v_b are iteratively determined by the appearing and disappearing of interpolation points at two scales. ρ_m and ρ_n are the binary design variables, representing the statuses of interpolation points during the optimization.

2.2. Robust topology optimization formulation

If material uncertainties for the elastic modulus and Poisson's ratio are subjected to $E \sim N(\mu_E, \sigma_E^2)$ and $\nu \sim N(\mu_\nu, \sigma_\nu^2)$, where μ_E and σ_E^2 denote the expectation and variance of the elastic modulus, and μ_ν and σ_ν^2 are the expectation and variance of the Poisson's ratio. The deterministic formulation defined in Eq. (1) can then be transformed to the following one:

$$\text{Minimize : } J(\rho, E, \nu) = \omega_1 \mu(C) + \omega_2 \sigma(C) \tag{2}$$

where $\mu(C)$ and $\sigma(C)$ are expectation and standard deviation of structural compliance, ω_1 and ω_2 correspond to the weight coefficients (1 in this study). Consider the uncertainties of applied loads described by unknown-but-bounded variables, the structural compliance can be described as an interval variable:

$$[C] = [\underline{C}, \bar{C}] = \{C_i | R | C_i \bar{C}_i, i = 1, 2, Lk\} \tag{3}$$

Then mean and deviation of interval compliance should be written as

$$C^m = (\underline{C} + \bar{C})/2, \quad C^d = (\bar{C} - \underline{C})/2 \tag{4}$$

The upper bound of the interval objective function, known as the worst-case condition, is usually considered as the robust objective function, such as

$$\text{Minimize : } J = (\rho, E, \nu, [p], [\theta]) = \mu(\bar{C}) + \sigma(\bar{C}) \tag{5}$$

Traditionally, all vertexes of interval parameters should be enumerated by comparison. However, this process is time consuming. With the help of ODUS method, this study transforms the RTO problem to a deterministic one with multiple cases, and the average performance of interval compliance can be used as a new objective function:

$$\begin{aligned}
 \text{Minimize : } J &= (\rho, E, v, [p], [\theta]) = \mu(\tilde{C}) + \sigma(\tilde{C}) \\
 \tilde{C}[z] &= \frac{1}{L} \sum_{i=1}^L U^T(z_i) K(z_i) U(z_i) \\
 \text{Subject to : } F^{(MA)} &= KU^{(MA)} \\
 V^{MA*} - \sum_{a=1}^S V_a v_a(\rho_m) &= 0 \\
 V^{MI*} - \sum_{b=1}^T V_b v_b(\rho_n) &= 0 \\
 \rho_m, \rho_n &= 0 \text{ or } 1
 \end{aligned} \tag{6}$$

where \tilde{C} indicates the average performance of structural compliance corresponding to the interval variable $[z]$. $\mu(\tilde{C})$ and $\sigma(\tilde{C})$ are expectation and standard variation related to \tilde{C} , and L is the selected sample numbers. Other parameters are consistent with the ones defined in Eq. (1).

2.3. Energy-based homogenization method

If periodic unit cell of material microstructure is small enough than the geometric size of the macrostructure, homogenization theory can give us a way to evaluate the effective properties of microstructures involved in the concurrent design of structures and materials [38,39]. This study adopts the energy-based homogenization method to predict the macroscopic equivalent elastic properties of material microstructures, which is based on the criterion of energy conservation with respect to stress and strain. Under the framework of linear elasticity theory, the macroscopic displacement of 2D microstructures periodically configured in the design space can be expressed as

$$s^t(x) = s_0(x, y) + \epsilon s_1(x, y) + \epsilon^2 s_2(x, y) + L \tag{7}$$

where $\epsilon = y/x$ is a scale factor, periodic unit cell will approach to be a point when $\epsilon \approx 0$. Leveraging the trade-off between computational efficiency and accuracy, this study only considers the first-order term in Eq. (7). One of the homogenized elastic tensor of E^2 can be obtained by averaging the strain energy:

$$\begin{aligned}
 E_{ijkl}^H &= \frac{1}{|Y|} \int_Y E_{pqrs} (\epsilon_{pq}^{0(ij)} - \epsilon_{pq}^{*(ij)}) (\epsilon_{rs}^{0(kl)} - \epsilon_{rs}^{*(kl)}) \\
 &\quad - \epsilon_{rs}^{*(kl)}) dY (i, j, k, l = 1, 2, L, D)
 \end{aligned} \tag{8}$$

where E_{pqrs} is an elastic tensor with respect to isotropic solid material, D denotes the design dimension of periodic unit cell, $\epsilon_{pq}^{0(ij)}$ and $\epsilon_{rs}^{0(kl)}$ are the initial unit test strain. The unknown item $\epsilon_{rs}^{*(kl)}$ is the Y -periodic solution of the following equilibrium equation:

$$\int_Y E_{ijrs} \epsilon_{rs}^{*(kl)} \frac{\partial w_i}{\partial y_j} dY = \int_Y E_{ijrs} \epsilon_{rs}^{0(kl)} \frac{\partial w_i}{\partial y_j} dY \tag{9}$$

where $\epsilon_{pq}^{*(ij)}$ can be also obtained in the same way owing to the symmetry of Eq. (9), w is the virtual displacement field. If a periodic unit cell is divided into N_e elements, the homogenized elastic property shown in Eq. (9) can be calculated through the finite element analysis and summation:

$$E_{ijkl}^H = \frac{1}{|Y|} \sum_{e=1}^{N_e} (u_e^{0(ij)} - u_e^{*(ij)})^T k_e (u_e^{0(kl)} - u_e^{*(kl)}) \tag{10}$$

where $u_e^{*(ij)}$ and $u_e^{(kl)}$ are elemental displacements to be solved, k_e is elemental stiffness matrix. If the induced unit strain fields expressed in brackets of Eq. (10) are written as $\epsilon_{pq}^{D(ij)}$ and $\epsilon_{rs}^{D(kl)}$, Eq. (10) should be abbreviated as follows in terms of elemental mutual energy:

$$E_{ijkl}^H = \frac{1}{|Y|} \sum_{e=1}^{N_e} (u_e^{D(ij)})^T k_e (u_e^{D(kl)}) \tag{11}$$

3. Hybrid uncertainty quantification method

One difficulty in solving the RTO problem given in Eq. (6) is how to efficiently quantify the hybrid uncertainties [29], this section proposes a novel ODUS-NIPCE method to simultaneously quantify the load and material uncertainties.

3.1. Odus method

3.1.1. Orthogonal decomposition

This study focuses on the linear elastic structure, uncertain force F_i in 2D scenarios can be expressed by a linear combination of horizontal and vertical force vectors, such as

$$F_i = [F_i^1, F_i^2]^T = [p_i \cos \theta_i, p_i \sin \theta_i]^T \tag{12}$$

where i denotes the i -th uncertainty force, F_i^1 and F_i^2 are horizontal and vertical components decomposed by uncertainty force, respectively. p_i and θ_i are load magnitude and direction, respectively. Fig. 1 shows the decomposition of two uncertainty forces in 2D scenarios.

The nodal force vector generated by F_i can be expressed by two unit forces, such as

$$R_i = [R_i^1, R_i^2]^T = [R_i^1 p_i \cos \theta_i, R_i^2 p_i \sin \theta_i]^T = [R_i^1, R_i^2]^T F_i \tag{13}$$

Correspondingly, the nodal displacement vector generated by F_i can be also expressed by the decomposed unit displacements in two directions:

$$U_i = [U_i^1, U_i^2]^T = [U_i^1, U_i^2]^T F_i \tag{14}$$

Suppose there are K uncertain loads, structural compliance should be expressed as:

$$\begin{aligned}
 C &= \sum_{i=1}^K U_i^T R_i = \sum_{i=1}^K \sum_{j=1}^K F_i^T [U_i^1, U_i^2]^T [R_j^1, R_j^2]^T F_j \\
 &\quad j = 1 \\
 &= \sum_{i=1}^K \sum_{j=1}^K F_i^T c_{ij} F_j
 \end{aligned} \tag{15}$$

Eq. (15) can be further separated into two parts using mathematical operations, such as

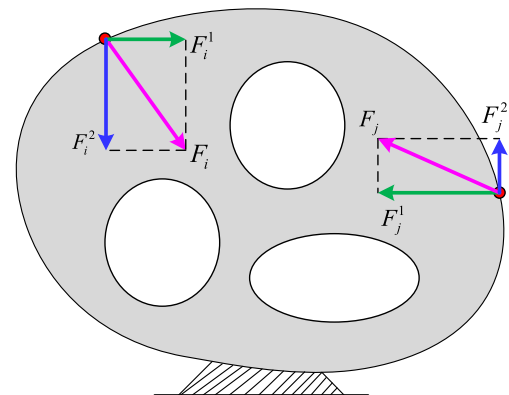


Fig. 1. Illustration for the decomposition of two uncertainty forces in 2D scenarios.

$$C = \sum_{i=1}^K F_i^k F_i^l c_{ii}^{kl} + 2 \sum_{i=2}^K \sum_{j=1}^{i-1} F_i^k F_j^l c_{ij}^{kl} \quad (16)$$

$$= \sum_{i=1}^K (p_i^k \cos \theta_i) (p_i^l \sin \theta_i) c_{ii}^{kl} + 2 \sum_{i=2}^K \sum_{j=1}^{i-1} (p_i^k \cos \theta_i) (p_j^l \sin \theta_j) c_{ij}^{kl}$$

The coefficients related to the uncertain forces F_i and F_j do not involve the finite element analysis, since their calculation processes are limited to mathematical operations, and c_{ij} is the mutual compliance with a size of 2×2 for each element, which is a deterministic one calculated by the product of unit force and unit displacement. To separate the uncertainty coefficients, a point function $t^s(\theta)$ is introduced to facilitate the following derivations:

$$t^s(\theta) = \begin{cases} \cos \theta, & \text{if } s = 1 \\ \sin \theta, & \text{if } s = 2 \end{cases} \quad (17)$$

Structural compliance should be further expressed as

$$C = \sum_{i=1}^K p_i^2 (t^k(\theta_i) \cdot t^l(\theta_i)) c_{ii}^{kl} + 2 \sum_{i=2}^K \sum_{j=1}^{i-1} p_i p_j (t^k(\theta_i) \cdot t^l(\theta_j)) c_{ij}^{kl} \quad (18)$$

where the coefficients pertaining to interval uncertainties are separated into two parts: one is related to load magnitude, the other is related to load direction.

3.1.2. Uniform sampling

\mathbf{R} signifies an arbitrary real set, and interval variables related to load magnitude and direction $p_i \in \mathbf{R}$ can be defined as two pairs of ordered real numbers, such as

$$\begin{cases} [p] = [p^l, p^r] = \{p_i \in \mathbf{R} | p_i^l < p_i < p_i^r, i = 1, 2, \dots, L\} \\ [\theta] = [\theta_i^l, \theta_i^r] = \{\theta_i \in \mathbf{R} | \theta_i^l < \theta_i < \theta_i^r, i = 1, 2, \dots, L\} \end{cases} \quad (19)$$

where p_i^l and p_i^r are the left and right bounds of load magnitude, respectively, θ_i^l and θ_i^r are the left and right bounds of load direction, respectively. If we select L samples equally spaced to calculate the structural compliance, p_i and θ_i can be naturally divided into $L-1$ subintervals, and p_{ik} and θ_{ik} related to the k -th sample p_{ik} should be expressed as

$$\begin{cases} p_{ik} = p_i^l + \frac{p_i^r - p_i^l}{M-1} \cdot (k-1) \\ \theta_{ik} = \theta_i^l + \frac{\theta_i^r - \theta_i^l}{M-1} \cdot (k-1) \end{cases} \quad (20)$$

To separate the magnitude uncertainty and directional uncertainty, Eq. (19) should be written as

$$\begin{cases} \tilde{C}_p = \sum_{i=1}^K a_1 (t^k(\theta_i) \cdot t^l(\theta_i)) c_{ii}^{kl} + 2 \sum_{i=2}^K \sum_{j=1}^{i-1} a_2 (t^k(\theta_i) \cdot t^l(\theta_j)) c_{ij}^{kl} \\ \tilde{C}_\theta = \sum_{i=1}^K p_i^2 b_1 c_{ii}^{kl} + 2 \sum_{i=2}^K \sum_{j=1}^{i-1} p_i p_j b_2 c_{ij}^{kl} \end{cases} \quad (21)$$

where the coefficients a_1 , a_2 , b_1 and b_2 defined in Eq. (21) can be obtained by the following formulations according to uniform sampling:

$$\begin{cases} a_1 = \frac{1}{L} \sum_{k=1}^L \sum_{i=1}^K \left(p_i^l + \frac{p_i^r - p_i^l}{L-1} \cdot (k-1) \right)^2 \\ a_2 = \frac{1}{L} \sum_{k=1}^L \sum_{i=1}^K \left(p_i^l + \frac{p_i^r - p_i^l}{L-1} \cdot (k-1) \right) \cdot \left(p_j^l + \frac{p_j^r - p_j^l}{L-1} \cdot (k-1) \right) \end{cases} \quad (22)$$

$$\begin{cases} b_1 = \frac{1}{L} \sum_{k=1}^L \sum_{i=1}^K t^k \left(\frac{\theta_i^r - \theta_i^l}{L-1} \cdot (k-1) \right) \cdot t^l \left(\frac{\theta_i^r - \theta_i^l}{L-1} \cdot (k-1) \right) \\ b_2 = \frac{1}{L} \sum_{k=1}^L \sum_{i=1}^K t^k \left(\frac{\theta_i^r - \theta_i^l}{L-1} \cdot (k-1) \right) \cdot t^l \left(\frac{\theta_j^r - \theta_j^l}{L-1} \cdot (k-1) \right) \end{cases} \quad (23)$$

Structural compliance related to the magnitude and direction of the uncertainty can be calculated through Eq. (21)-(23). It should be noted that sample numbers of load magnitude and direction can be different during the optimization, according to the accuracies. When load uncertainties exist in both the magnitude and direction, structural compliance can be analytically expressed as

$$\tilde{C}_{p\theta} = \sum_{i=1}^K a_1 b_1 c_{ii}^{kl} + \sum_{i=2}^K \sum_{j=1}^{i-1} a_2 b_2 c_{ij}^{kl} \quad (24)$$

3.2. Nipce method

In traditional finite element method, the relationship between material uncertainty and structural response is implicitly expressed, so the RTO problem defined in Eq. (6) cannot be solved directly. Although the Monte Carlo simulation can be used to quantify probability uncertainties, the calculational cost is prohibitive. This study introduces the NIPCE model to calculate the statistical moments of the robust objective functions, which is based on the rigorous Polynomial Chaos theory. NIPCE is able to describe any input and output probability relationships, without involving the traditional topology optimization framework [40]. When the considered uncertainties subjected to Gaussian distributions, their orthogonal basis corresponding to NIPCE should be the Hermit polynomials, such as

$$Y(\theta) = \alpha_0 H_0 + \sum_{i_1} \alpha_{i_1} H_1(\xi_{i_1}(\theta)) + \sum_{i_1} \sum_{i_2=1}^{i_1} \alpha_{i_1 i_2} H_2(\xi_{i_1}(\theta), \xi_{i_2}(\theta)) + \sum_{i_1} \sum_{i_2=1}^{i_1} \sum_{i_3=1}^{i_2} \alpha_{i_1 i_2 i_3} H_3(\xi_{i_1}(\theta), \xi_{i_2}(\theta), \xi_{i_3}(\theta)) + \dots \quad (25)$$

where θ is an arbitrary random variable, $H_n(\xi_{i_1}(\theta), \dots, \xi_{i_n}(\theta))$ denotes the Hermit orthogonal polynomial with n order, $\xi_{i_n}(\theta)$ and $\alpha_{i_1 i_2 \dots i_n}$ are the standard Gaussian random variable and NIPCE coefficient, respectively. For an easy expression, Eq. (25) can be abbreviated as

$$Y = \sum_{i=0}^{\infty} \tilde{\alpha}_i \psi_i(\xi) \quad (26)$$

where $\tilde{\alpha}_i$ and ψ_i correspond to the NIPCE coefficients and orthogonal basis functions with different orders. Generally, Eq. (26) should be truncated in practical applications because of its infinities, the truncated NIPCE model with p order should be expressed as

$$Y \approx \tilde{Y} = \sum_{i=0}^p \tilde{\alpha}_i \psi_i(\xi) \quad (27)$$

this study employs the second-order truncation of the Hermit polynomial expansion. Owing to the orthogonality of polynomials, their tensor products should be written as

$$\langle \psi_i(\xi) \psi_j(\xi) \rangle = \langle \psi_i^2(\xi) \rangle \delta_{ij} \quad (28)$$

where $\langle \cdot \rangle$ represents inner product, and δ_{ij} is the Kronecker delta function.

$$\delta_{ij} = \begin{cases} 1, & i = j \\ 0, & i \neq j \end{cases} \quad (29)$$

The following inner product to be solved is related to Gaussian random variables, because ξ is a standard Gaussian random variable [41].

$$\langle f(\xi) g(\xi) \rangle = \int f(\xi) g(\xi) W(\xi) d\xi \quad (30)$$

The weight function related to random variables should be calculated by:

$$W(\xi) = e^{-\xi^T \xi / 2} \quad (31)$$

To obtain satisfactory accuracy, this paper adopts twice as many sample points as the unknown NIPCE coefficients. On substituting the sample points $\xi^S = [\xi_1^S, \dots, \xi_N^S]^T$ and their corresponding function responses $\mathbf{G} = [g(X_1^S), \dots, g(X_N^S)]^T$ in Eq. (27), yields

$$\begin{bmatrix} \psi_0(\xi_1^S) & \psi_1(\xi_1^S) & \dots & \psi_p(\xi_1^S) \\ \psi_0(\xi_2^S) & \psi_1(\xi_2^S) & \dots & \psi_p(\xi_2^S) \\ \vdots & \vdots & \ddots & \vdots \\ \psi_0(\xi_N^S) & \psi_1(\xi_N^S) & \dots & \psi_p(\xi_N^S) \end{bmatrix} \begin{bmatrix} \hat{\alpha}_0 \\ \hat{\alpha}_1 \\ \vdots \\ \hat{\alpha}_p \end{bmatrix} = \begin{bmatrix} g(X_1^S) \\ g(X_2^S) \\ \vdots \\ g(X_N^S) \end{bmatrix} \quad (32)$$

Eq. (32) can be abbreviated as

$$\psi \hat{\alpha} = \mathbf{G} \quad (33)$$

According to the least square's method, NIPCE coefficients should be calculated by

$$\hat{\alpha} = (\psi^T \psi)^{-1} \psi^T \mathbf{G} \quad (34)$$

NIPCE models can be successfully constructed when their coefficients are obtained, the previous two NIPCE coefficients correspond to the expectation and standard deviation of the objective function, which can be written as

$$\begin{cases} \mu_z = \hat{\alpha}_0 \\ \sigma_z = \sqrt{\sum_{i=1}^k \hat{\alpha}_i^2 \langle \psi_i^2 \rangle} \end{cases} \quad (35)$$

4. Sensitivity analysis and algorithm implementation

To solve the RTO problem defined in Eq. (6) using the mature optimization algorithm, the sensitivities with respect to design variables should be obtained [42]. In BETO, the required volume fractions at two scales can be satisfied automatically [43], so there is no need to calculate the derivatives of the volume constraints with respect to design variables. Since the interpolation points $\rho = [\rho_m, \rho_n]$ are discontinuous, this section defines elemental densities $\mathbf{x} = [x_a, x_b]$ as auxiliary variables to facilitate derivations.

4.1. Macroscopic sensitivity

According to the chain rule, the derivative of RTO objective function with respect to the macroscopic design variables can be written as

$$\frac{\partial J}{\partial x_a} = \left(\frac{\partial \hat{\alpha}_0}{\partial x_a} + \frac{1}{\sigma_c} \sum_{q=1}^k \hat{\alpha}_q \frac{\partial \hat{\alpha}_q}{\partial x_a} \right) \frac{\partial \tilde{C}}{\partial x_a} \quad (36)$$

where $\partial \hat{\alpha}_0 / \partial x_a$ and $\partial \hat{\alpha}_q / \partial x_a$ are the derivatives of the 0-order and q -order coefficients related to macroscopic design variables, σ_c is the standard deviation of structural compliance to be solved, $\hat{\alpha}_q$ denotes the q -th NIPCE coefficient of macroscopic sensitivity, $\partial \tilde{C} / \partial x_a$ is the derivative of structural compliance related to macroscopic design variables, $k = 2$ is the order of polynomial chaos expansion. This section will derive $\partial \hat{\alpha}_0 / \partial x_a$, $\partial \hat{\alpha}_q / \partial x_a$ and $\partial \tilde{C} / \partial x_a$, respectively.

First, the partial derivative of the robust objective function with respect to the macroscopic design variables can be directly represented as

$$\frac{\partial \tilde{C}}{\partial x_a} = \sum_{q=0}^k \frac{\partial \hat{\alpha}_q}{\partial x_a} \psi_q \quad (37)$$

Second, the macroscopic sensitivity will be regarded as another probability distribution, and can be expressed as a summation of orthogonal basis functions according to NIPCE:

$$d(\rho_m) = \sum_{q=0}^k \hat{\beta}_q \psi_q \quad (38)$$

By comparing Eq. (37) and (38), it is easy to see that $\partial \hat{\alpha}_q / \partial x_a$ given in Eq. (37) can be obtained by using the sensitivity expansion as follows:

$$\frac{\partial \hat{\alpha}_q}{\partial x_a} = \hat{\beta}_q \quad (39)$$

On substituting Eq. (39) into Eq. (36), the sensitivity of the robust objective function with respect to the macroscopic design variables should be written as

$$\frac{\partial J}{\partial x_a} = \left(\hat{\beta}_0 + \frac{1}{\sigma_c} \sum_{q=1}^k \hat{\alpha}_q \hat{\beta}_q \right) \frac{\partial \tilde{C}}{\partial x_a} \quad (40)$$

where $\partial \tilde{C} / \partial x_a$ can be easily obtained with the ODUS method, because they are explicit expressions for the magnitude uncertainty, directional uncertainty and combined uncertainties, such as

$$\begin{cases} \frac{\partial \tilde{C}}{\partial x_a} = \sum_{i=1}^Y a_1 (t^k(\theta_i) \cdot t^l(\theta_i)) c_{ii}^{kl} \frac{\partial c_{ii}^{kl}}{\partial x_a} + 2 \sum_{i=2}^Y \sum_{j=1}^{i-1} a_2 (t^k(\theta_i) \cdot t^l(\theta_j)) \frac{\partial c_{ij}^{kl}}{\partial x_a} \\ \frac{\partial \tilde{C}}{\partial x_a} = \sum_{i=1}^Y p_i^2 b_1 \frac{\partial c_{ii}^{kl}}{\partial x_a} + 2 \sum_{i=2}^Y \sum_{j=1}^{i-1} p_i p_j b_2 \frac{\partial c_{ij}^{kl}}{\partial x_a} \\ \frac{\partial \tilde{C}}{\partial x_a} = \sum_{i=1}^Y a_1 b_1 \frac{\partial c_{ii}^{kl}}{\partial x_a} + 2 \sum_{i=2}^Y \sum_{j=1}^{i-1} a_2 b_2 \frac{\partial c_{ij}^{kl}}{\partial x_a} \end{cases} \quad (41)$$

All parameters defined in Eq. (41) are consistent with those given in Section 3.1. For self-compliance and mutual compliance which have nothing to do with uncertainties, their derivatives related to macroscopic design variables can be expressed as [14]

$$\begin{cases} \frac{\partial c_{ii}^{kl}}{\partial x_a} = [v_a + (1 - v_a)x_{\min}] (\mathbf{u}_i^k)^T \mathbf{k}_e \mathbf{u}_i^l \\ \frac{\partial c_{ij}^{kl}}{\partial x_a} = [v_a + (1 - v_a)x_{\min}] (\mathbf{u}_i^k)^T \mathbf{k}_e \mathbf{u}_j^l \end{cases} \quad (42)$$

where v_a is the a -th elemental volume, x_{\min} is a low density assigned to void elements, \mathbf{k}_e is elemental stiffness matrix of solid element filled with microstructure. \mathbf{u}_i and \mathbf{u}_j are displacements to be solved for the i -th and j -th element.

4.2. Microscopic sensitivity

In this study, the design space of the macrostructure is periodically configured with one identical material microstructure, so there is only one type of microscopic sensitivity to be calculated. Similar to Eq. (40), the derivative of the robust objective function with respect to microscopic design variables should be written as

$$\frac{\partial J}{\partial x_b} = \left(\hat{\zeta}_0 + \frac{1}{\sigma_c} \sum_{q=1}^k \hat{\gamma}_q \hat{\zeta}_q \right) \frac{\partial \tilde{C}}{\partial x_b} \quad (43)$$

where x_b denotes any of the microscopic design variables, $\hat{\zeta}_0$ and $\hat{\zeta}_q$ are derivatives of the 0-order and q -order NIPCE coefficients related to microscopic design variables, $\hat{\gamma}_q$ is the q -order NIPCE coefficient of microscopic sensitivity, $\partial \tilde{C} / \partial x_b$ is the derivative of structural

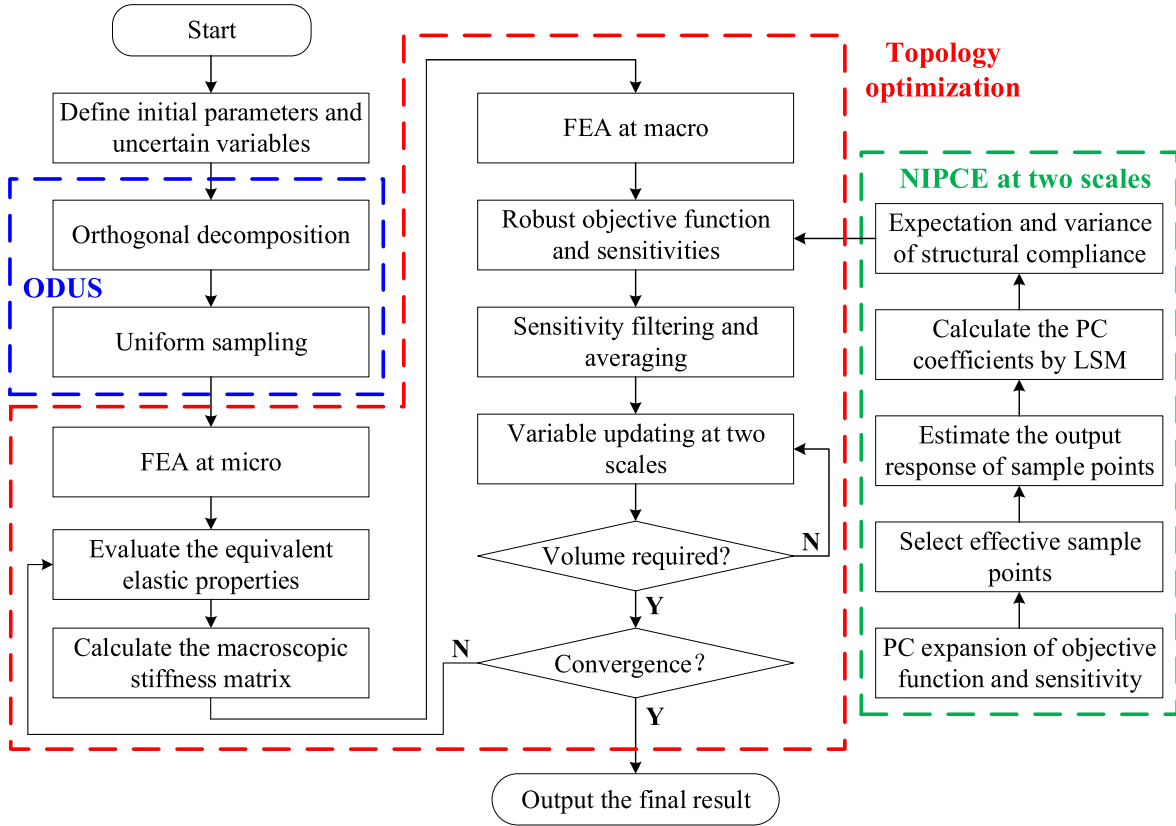


Fig. 2. Flow chart of algorithm implementation.

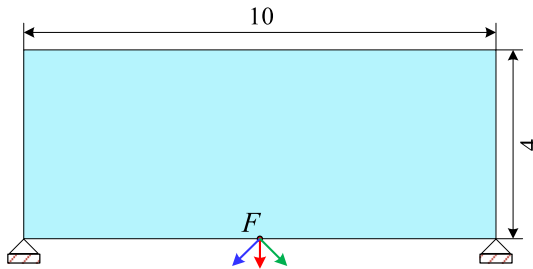


Fig. 3. Boundary conditions for a Michell-type structure.

$$\begin{cases} \frac{\partial c_{ii}^{kl}}{\partial x_b} = \sum_{a=1}^S [v_a + (1 - v_a)x_{\min}] (\mathbf{u}_i^k)^T \frac{\partial \mathbf{k}_e}{\partial x_b} \mathbf{u}_i^l \\ = \sum_{a=1}^S [v_a + (1 - v_a)x_{\min}] (\mathbf{u}_i^k)^T \int_A \mathbf{B}^T \frac{\partial E^H}{\partial x_b} \mathbf{B} dA \mathbf{u}_i^l \\ \frac{\partial c_{ij}^{kl}}{\partial x_b} = \sum_{a=1}^S [v_a + (1 - v_a)x_{\min}] (\mathbf{u}_i^k)^T \frac{\partial \mathbf{k}_e}{\partial x_b} \mathbf{u}_j^l \\ = \sum_{a=1}^S [v_a + (1 - v_a)x_{\min}] (\mathbf{u}_i^k)^T \int_A \mathbf{B}^T \frac{\partial E^H}{\partial x_b} \mathbf{B} dA \mathbf{u}_j^l \end{cases} \quad (44)$$

where \mathbf{k}_e is elemental stiffness matrix depended by the microstructural configuration, E^H is the equivalent elastic property of material microstructure, other parameters are the same as the macroscopic sensitivity explained in Section 4.1, \mathbf{B} is the stress-strain matrix.

The derivative of the equivalent elastic tensor related to the macroscopic design variable can be expressed by [46]

$$\frac{\partial E^H}{\partial x_b} = [v_b + (1 - v_b)x_{\min}] \frac{1}{|Y|} (\mathbf{u}_b^{A(ij)})^T \mathbf{k}_0 \mathbf{u}_b^{A(kl)} \quad (45)$$

where \mathbf{k}_0 is the elemental stiffness matrix related to base material, which can be calculated by the Gaussian integration. On substituting Eq. (44–45) into Eq. (43), finally the sensitivity of the robust objective function related to the microscopic design variables can be obtained.

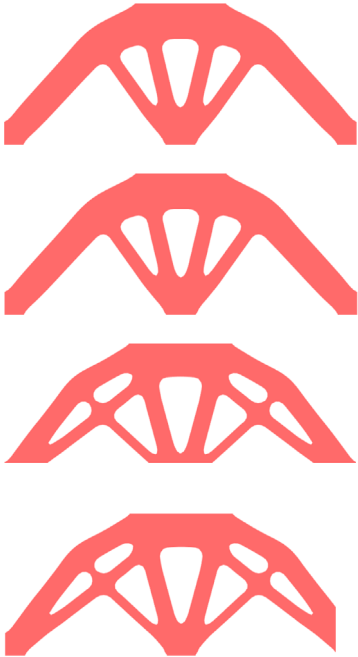
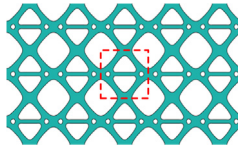

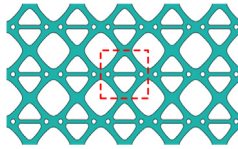

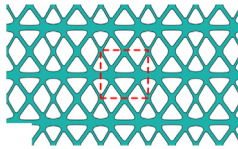

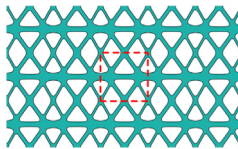

compliance related to microscopic design variables. Obviously, $\hat{\zeta}_0$, $\hat{\gamma}_q$ and $\hat{\zeta}_q$ can be obtained by NIPCE.

Additionally, the derivatives of the self-compliance c_{ii}^{kl} and mutual compliance c_{ij}^{kl} related to microscopic design variables can also be obtained. Under deterministic parameters, the sensitivity is equivalent to the summation of the derivatives of the objective function related to the macroscopic design variables as [37]:

Table 1
Parameters under different cases.

Analysis case		ρ	θ	E	ν
Case 1	Deterministic	2	-90°	1	0.3
Case 2	Magnitude uncertainty	[1.6, 2.4]	-90°	1	0.3
Case 3	Directional uncertainty	2	$[-105^\circ, -75^\circ]$	1	0.3
Case 4	Hybrid uncertainty	[1.6, 2.4]	$[-105^\circ, -75^\circ]$	1	0.3

Table 2
Topological results and equivalent properties of the Michell-type structure.

Macrostructure	Periodic arrays	Microstructure	Equivalent properties
	Case 1 		$\begin{bmatrix} 0.1840 & 0.0928 & 0 \\ 0.0928 & 0.1628 & 0 \\ 0 & 0 & 0.0802 \end{bmatrix}$
	Case 2 		$\begin{bmatrix} 0.1840 & 0.0928 & 0 \\ 0.0928 & 0.1628 & 0 \\ 0 & 0 & 0.0802 \end{bmatrix}$
	Case 3 		$\begin{bmatrix} 0.1866 & 0.0788 & 0 \\ 0.0788 & 0.1964 & 0 \\ 0 & 0 & 0.0751 \end{bmatrix}$
	Case 4 		$\begin{bmatrix} 0.1866 & 0.0788 & 0 \\ 0.0788 & 0.1964 & 0 \\ 0 & 0 & 0.0751 \end{bmatrix}$

4.3. Algorithm implementation

To avoid the potential numerical instabilities, previous experiences show that filter operation is a simple but efficient numerical skill to stabilize the optimization process [44], which can be written as

$$\hat{\alpha}_b = \sum_{a=1}^T \omega_{ab} \alpha_a / \sum_{a=1}^T \omega_{ab} \quad (46)$$

where $\hat{\alpha}_b$ is the sensitivity number related to the b -th node, T signifies total number of nodes interpolated in the design domain, ω_{ab} is a linear weighting factor to measure the contribution of elemental sensitivity α_a to $\hat{\alpha}_b$. To be precise, the greater the distance between element a and node b , the greater the influence of α_a on $\hat{\alpha}_b$. ω_{ab} can be expressed as

$$\omega_{ab} = \max(r_{\min} - r(a, b), 0) \quad (47)$$

where r_{\min} is a specified filter radius, $r(a, b)$ is the distance between element a and node b .

Although the sensitivity filtering is adopted, the objective function and structural topology may still experience convergence issue. To further stabilize the optimization process, nodal sensitivities of two adjacent iterations will be averaged by

$$\left(\bar{\alpha}_b\right)_z = \frac{\left(\hat{\alpha}_b\right)_z + \left(\bar{\alpha}_b\right)_{z-1}}{2} \quad (48)$$

where $\left(\bar{\alpha}_b\right)_z$ is the averaged sensitivity number of element b in the z -th iteration, $\left(\hat{\alpha}_b\right)_z$ is the filtered sensitivity number in the z -th iteration, $\left(\bar{\alpha}_b\right)_{z-1}$ is the averaged sensitivity number in the $(z-1)$ -th iteration. Obviously, nodal sensitivity in this iteration contains all the sensitivity information of the previous iterations.

In BETO, the target volume to be given before each iteration will be used to determine the amount of material that will be removed:

$$V_z = \min[V_{z-1}(1 - er), V^*] \quad (49)$$

where V_z and V_{z-1} denote the structural volumes in the z -th and $(z-1)$ -th iterations, er is the evolutionary ratio, V^* is the required volume. It is noted that Eq. (46) to (49) need to be applied at two scales separately. Additionally, convergence should also be defined to terminate the whole optimization process, such as

$$error = \left(\left| \sum_{l=1}^S (C_{z-l+1} - C_{z-S-l+1}) \right| / \sum_{l=1}^S C_{z-l+1} \right) \leq \tau \quad (50)$$

where C_{z-l+1} and $C_{z-S-l+1}$ are the structural compliances in the $(z-l+1)$ -th and $(z-S-l+1)$ -th iterations, respectively, z is the current iteration number. $S = 5$ indicates that the objective function needs to iterate at least 10 times before termination of the algorithm. τ is the specified error accuracy, which is selected as 0.01% in this paper.

Algorithm implementation for the robust design of structure and material microstructure is given in Fig. 2. It is easy to see that the ODUS procedure is implement in a single loop, independent of finite element analysis, this saves a lot of computational costs and enables the algorithm to deal with large-scale optimization problems. The NIPCE quantification process related to material uncertainties is not involved in the topology optimization loop, which works like a black box. It should be noted that both the robust objective function and sensitivities are evaluated by using the NIPCE models that have different coefficients.

5. Numerical examples

This section provides 2D and 3D examples to discuss load and material uncertainties on the concurrent designs. For a fair com-

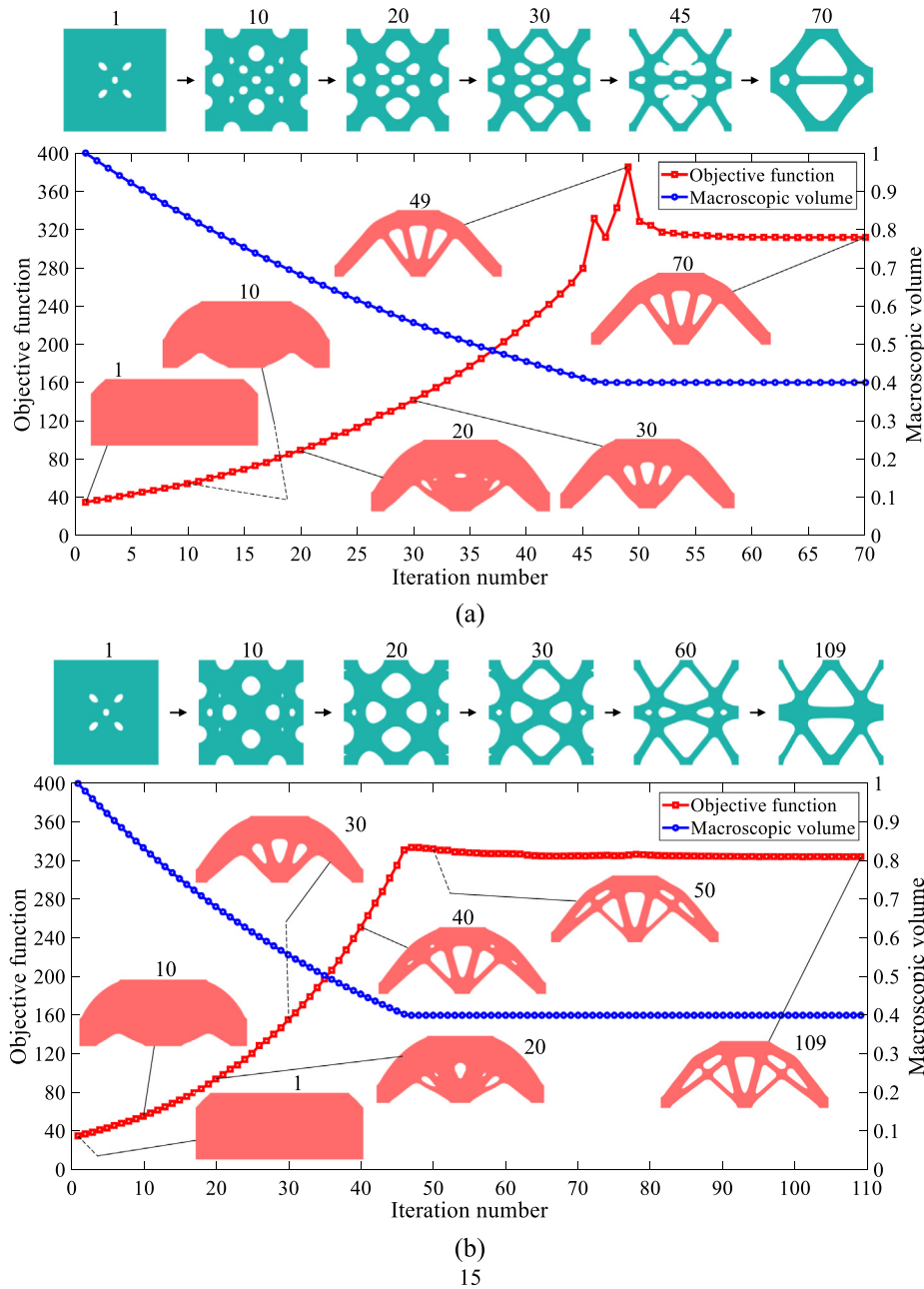


Fig. 4. Iteration curves related to case 1 and case 4. (a) Case 1; (b) Case 4.

Table 3
Numerical results of the Michell-type structure.

Uncertainty case	Deterministic condition			Robust condition		
	Maximum compliance	Mean compliance	CV	Maximum compliance	Mean compliance	CV
Case 2	448.9584	315.9833	0.3846	448.9584	315.9378	0.3846
Case 3	500.1573	375.2122	0.2320	361.3750	319.8637	0.0965
Case 4	703.7292	379.9789	0.5568	515.0030	324.1819	0.4584

parison, the scanning method is employed to calculate the maximum and average value of deterministic solutions, when subject to the same uncertainties considered in robust conditions. This study defines a normalized index to evaluate the structural robust-

ness, which contains both the maximum compliance C^{\max} and minimum compliance C^{\min} related to interval uncertainties, such as

$$CV = \frac{C^{\max} - C^{\min}}{C^{\max} + C^{\min}} \quad (51)$$

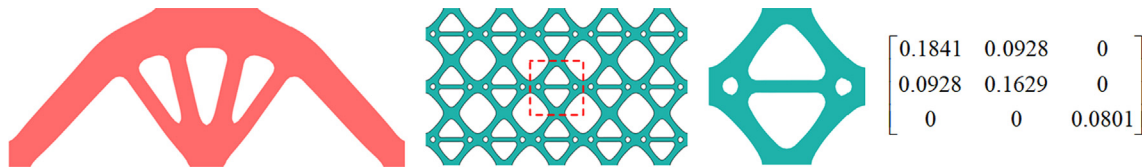


Fig. 5. Design results under material uncertainty.

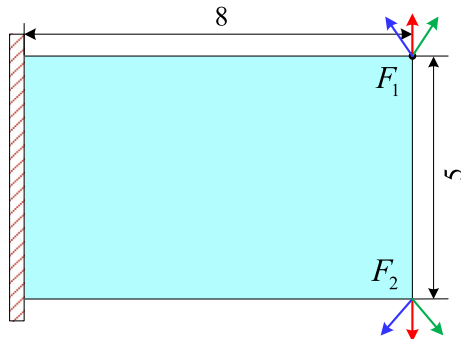


Fig. 6. Boundary conditions for cantilever beam.

5.1. Michell-type structure

A Michell-type structure is shown in Fig. 3. To discuss single load and material uncertainties on the design of structure and material microstructure. The two-scale design domains are set to 10×4 and 0.1×0.1 (dimensionless), and with 100×40 and 40×40 quadrilateral elements are used, respectively. Four cases including deterministic, magnitude uncertainty, directional uncertainty and hybrid uncertainty are considered, their parameter settings are listed in Table 1. P and θ are the load magnitude and load direction, respectively; E and ν are the elastic modulus and Poisson's ratio, respectively. Additionally, filter radiuses at two scales are set to 3, and volume ratios at two scales are set to 0.4. Table 1 lists topological results of structures and material microstructures, and the equivalent properties. Fig. 4 gives the convergence curves related to case 1 and case 4, and the numerical results under uncertain cases are listed in Table 3.

As illustrated in Table 2, the obtained topologies at two scales possess distinct and smooth boundaries. In case 1, macrostructural topology exhibits a semicircular arc configuration, four supports between force and arc are symmetrically distributed. The microstructure appears like a diamond with horizontal supports, with the compression resistance better than the shear resistance. This compares well with the macroscopic boundary condition. In case 2, topological designs and equivalent properties are the same with case 1, showing that magnitude uncertainty has little effect on the concurrent designs. In case 3, some porous materials transform to diagonal supports, to resist the load uncertainty in the horizontal direction. Microstructural topology is completely different from the previous two cases. Furthermore, the tensile and com-

pression performances in two main stress directions are improved. In case 4, topological solutions and equivalent properties are the same as the corresponding ones under directional uncertainty. It is easy to find that directional uncertainty affects the concurrent designs more than magnitude uncertainty when single load is applied.

As given in Table 3, in case 3 and case 4, robust results are smaller than the corresponding deterministic ones; especially for CV in case 3, where the robust value is 0.416 times of that under deterministic condition. In case 2 related to magnitude uncertainty, numerical results under deterministic and robust conditions are almost the same, which illustrates that directional uncertainty affect the concurrent designs more.

As shown in Fig. 4, volume ratios converge to the prescribed values stably, and the algorithm terminates within 110 iterations, which shows the BETO method has a good efficiency to implement concurrent designs. It should be noted that two-scale volume ratios are always consistent, owing to the same amounts of material removed in each iteration. Moreover, the objective function in case 1 shocks at the step 49, because the microstructure undergoes a major change at this step, even if the corresponding macrostructural topology evolved steadily. Case 4 related to hybrid uncertainty is stable enough during the whole optimization.

Subsequently, the influence of material uncertainty on the concurrent designs is analyzed. Elastic modulus and Poisson's ratio are assumed to subject to Gaussian distributions $E \sim N(1, 0.11^2)$ and $\nu \sim N(0.3, 0.04^2)$, respectively. Other parameter settings are the same as case 1, design results under material uncertainties are shown in Fig. 5. It is easy to find that there are little differences between material uncertainty and deterministic solutions, which shows that material uncertainty has little effect on the concurrent stiffness designs, compared to the topological optimization of metamaterial design reported in [41].

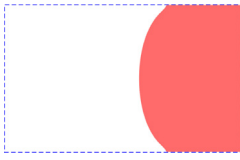
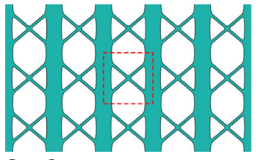

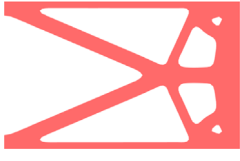
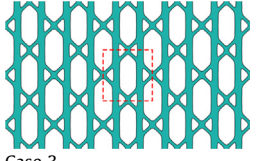


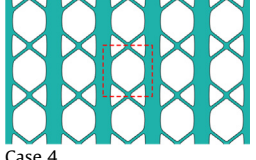


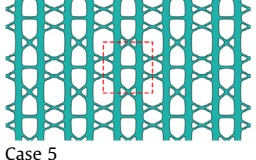


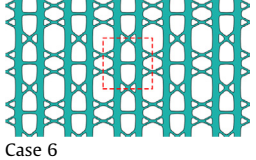

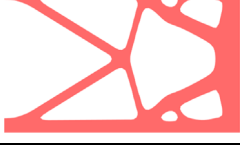
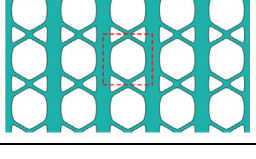

5.2. Cantilever beam

This example provides a cantilever beam to illustrate the influence of multiple loads and material uncertainties on the concurrent designs, loads and boundary conditions are shown in Fig. 6. The considered design domains at two scales are 8×5 and 0.1×0.1 , their mesh sizes are discretized as 80×50 and 40×40 , respectively. Six cases in Table 4 are analyzed, including deterministic, magnitude uncertainty, asymmetrical magnitude, directional uncertainty, asymmetry direction and hybrid uncertainty. Volume fractions at two scales are set to 0.4, two-scale filter radiuses are equal to 3 and 2, respectively. Table 5 lists topological

Table 4
Parameter settings for cantilever beam.

		p	θ	E	ν
Case 1	Deterministic	3	-90°	1	0.3
Case 2	Magnitude uncertainty	[2.5, 3.5]	-90°	1	0.3
Case 3	Asymmetrical magnitude asymmetry	[3, 3.5]	-90°	1	0.3
Case 4	Directional uncertainty	3	$[-105^\circ, -75^\circ]$	1	0.3
Case 5	Asymmetry direction	3	$[-90^\circ, -75^\circ]$	1	0.3
Case 6	Hybrid uncertainty	[2.5, 3.5]	$[-105^\circ, -75^\circ]$	1	0.3

Table 5
Topological design and equivalent elastic properties for cantilever beam.

Macrostructure	Periodic arrangements	Microstructure	Equivalent properties
	Case 1 		$\begin{bmatrix} 0.0668 & 0.0392 & 0 \\ 0.0392 & 0.3338 & 0 \\ 0 & 0 & 0.0392 \end{bmatrix}$
	Case 2 		$\begin{bmatrix} 0.0671 & 0.0441 & 0 \\ 0.0441 & 0.3216 & 0 \\ 0 & 0 & 0.0523 \end{bmatrix}$
	Case 3 		$\begin{bmatrix} 0.0796 & 0.0409 & 0 \\ 0.0409 & 0.3260 & 0 \\ 0 & 0 & 0.0380 \end{bmatrix}$
	Case 4 		$\begin{bmatrix} 0.1303 & 0.0366 & 0 \\ 0.0366 & 0.3083 & 0 \\ 0 & 0 & 0.0324 \end{bmatrix}$
	Case 5 		$\begin{bmatrix} 0.1286 & 0.0364 & 0 \\ 0.0364 & 0.3108 & 0 \\ 0 & 0 & 0.0332 \end{bmatrix}$
	Case 6 		$\begin{bmatrix} 0.1236 & 0.0433 & 0 \\ 0.0433 & 0.3003 & 0 \\ 0 & 0 & 0.0326 \end{bmatrix}$

solutions and equivalent properties. Fig. 7 depicts the convergence curves related to case 2 and case 6, and numerical results are listed in Table 6.

As shown in Table 5, porous materials in case 1 distribute dominantly on the right side of the macrostructure, and there is not much material between the macrostructure and the left support. The compression resistance in the vertical direction is 0.3338, which is much larger than that of 0.0668 in the horizontal direction, this aligns well with the macroscopic boundary condition.

Case 2 possesses support performances in both the horizontal and vertical directions. The two vertical supports are moved from two sides to the middle location of the microstructure, and the diamond-shaped components are enclosed to strength its mechanical performance. The pincer-shaped macrostructure, periodic arrangements, microstructures, and the equivalent properties obtained in case 3 are different from case 2, which illustrates the asymmetry of magnitude uncertainty has an influence on the multi-scale design.

In case 4, two-scale topological designs are completely different from the deterministic ones, macrostructural resistance in horizontal direction has been significantly enhanced, because more

materials appear to resist the horizontal force due to the directional uncertainty. In case 5, two-scale topological designs, periodic arrangements and equivalent properties exhibit little difference with case 4, which shows that the symmetry of the directional uncertainty has limit effect on the concurrent design.

In case 6, horizontal components appear more than the deterministic design to resist the hybrid uncertainty, the obtained macrostructure has support performances in both the horizontal and vertical directions, demonstrating that robust design is better than the deterministic one.

As illustrated in Table 6, the maximum compliances, mean compliances and CV values under deterministic condition are larger than the corresponding robust ones, especially for case 2 and case 3 related to the magnitude uncertainty. Their compliances reach up to 100 billion under deterministic condition, which explains that the robust designs are better than the deterministic ones. In case 4 and case 5 related to directional uncertainty, the CV values under the deterministic condition attain the maximum value 1, whereas the robust ones are 0.2408 and 0.1832, respectively, which illustrates that the deterministic structure is unstable under the directional uncertainty. In case 6, the deterministic CV value is

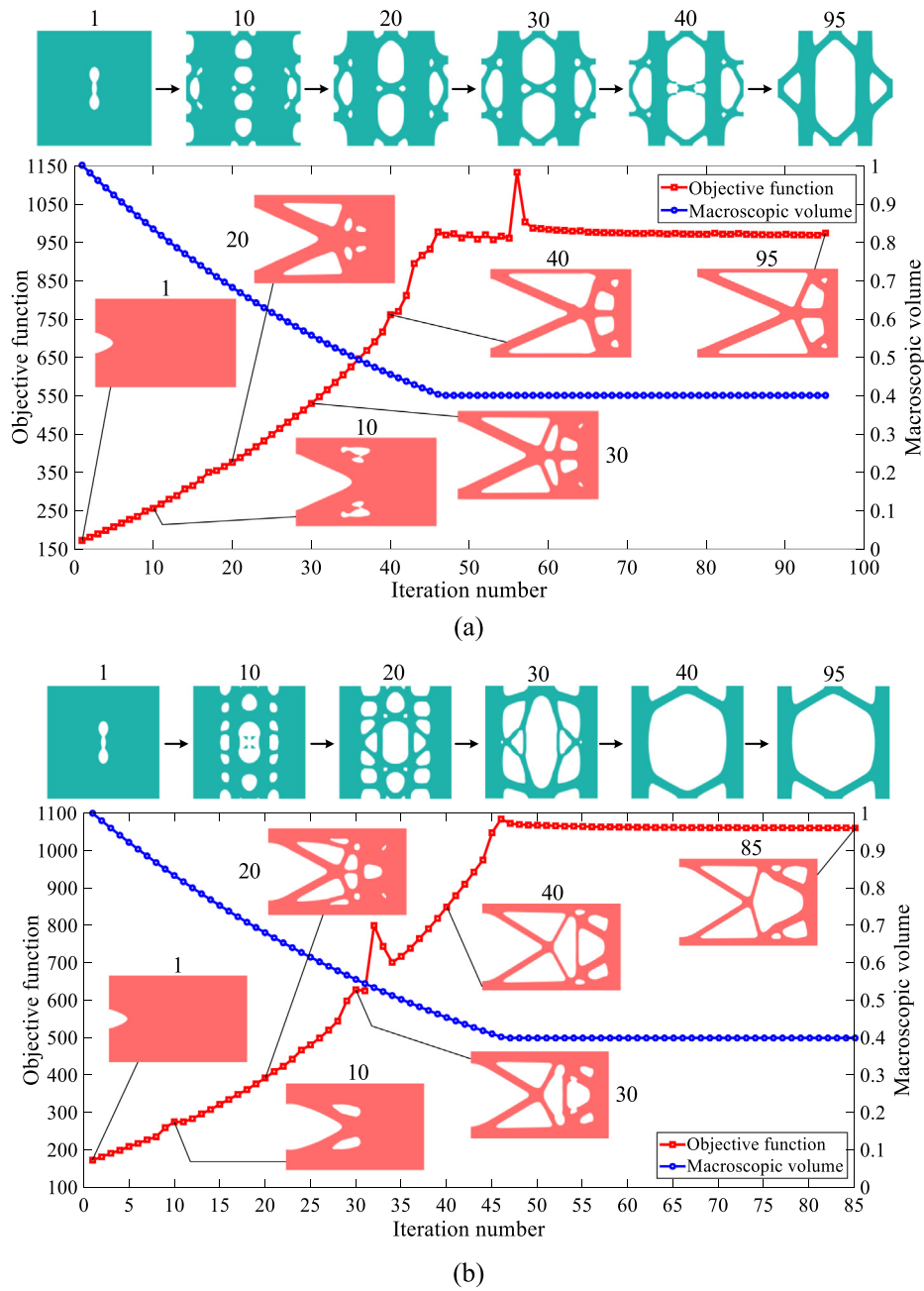


Fig. 7. Iteration histories related to case 2 and case 6. (a) Case 2; (b) Case 6.

Table 6
Numerical results of the cantilever beam.

Uncertainty case	Deterministic condition			Robust condition		
	Maximum compliance	Mean compliance	CV	Maximum compliance	Mean compliance	CV
Case 2	3.21e12	1.75e12	0.6223	1662.1102	973.0096	0.4838
Case 3	2.70e12	2.00e12	0.323	1202.7563	987.5978	0.1920
Case 4	3.60e10	1.21e10	1	1172.5711	874.0476	0.2408
Case 5	3.60e10	1.21e10	1	1166.9638	862.4014	0.1832
Case 6	2.44e11	1.01e11	0.8228	1359.0403	1060.5799	0.2657

3.1 times of that under the robust condition, demonstrating that robust design is better.

As illustrated in Fig. 7, the algorithm converges to the optimal designs within 100 iterations, iteration curves of volume fractions are smooth enough to reach the specified values. Both the objective

functions in Fig. 7 (a) and Fig. 7 (b) experience some shocks during the optimization, which indicate dramatic evolutions in microstructures, demonstrating the effectiveness of the proposed algorithm on the concurrent designs.

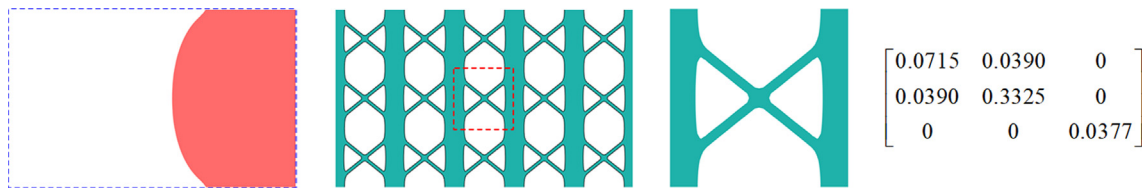


Fig. 8. Design results under material uncertainty.

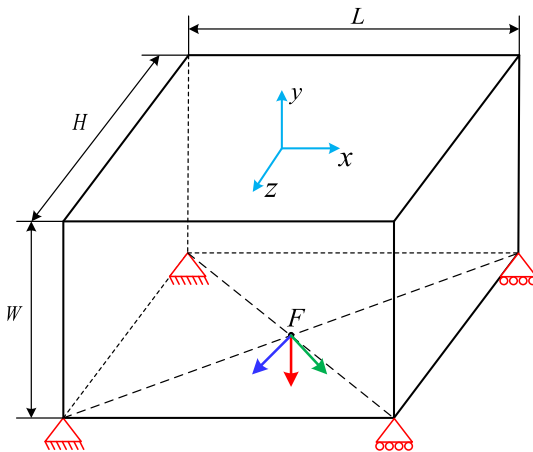


Fig. 9. Load and boundary condition of 3D Michell structure.

Subsequently, the influence of the material uncertainty on the concurrent designs related to multiple loads are investigated. Elastic modulus and Poisson’ ratio uncertainties are assumed to have the Gaussian distributions $E \sim N(1, 0.11^2)$ and $\nu \sim N(0.3, 0.04^2)$, respectively. Other parameter settings are the same as case 1. Design results under the material uncertainty are shown in Fig. 8. Two-scale topological designs, periodic arrangements and microstructure are similar to deterministic results. The tensile and compression performance in the horizontal direction is 0.0715, a little bigger than that of 0.0668 under the deterministic condition. This demonstrates that material uncertainty has little effect on the concurrent designs when related to multiple loads.

5.3. 3D Michell structure

This example provides a 3D Michell structure illustrated in Fig. 9, design domains at two scales are set to $L \times W \times H = 3 \times 2 \times 3$ and $0.1 \times 0.1 \times 0.1$, discretized as $30 \times 20 \times 30$ and $20 \times 20 \times 20$ elements, respectively. In two scales, the prescribed volume fractions are set to 20% and 30%, filter radiuses are set to 3 and 2, respectively. Three cases are considered, whose parameter settings are listed in Table 7, topological designs and equivalent elastic properties are shown in Table 8, iteration curves corresponding to case 2 are given in Fig. 10. Additionally, Table 9 exhibits numerical results under uncertain cases.

As illustrated in Table 8, topological designs at two scales possess clear and smooth boundaries in implementing 3D concurrent

designs. In case 1, the upper and lower sides of the macrostructure are connected by four diagonal braces, with no horizontal components between the fixed constraints. However, other three sides are distributed with horizontal components to resist the load uncertainties, and microstructure seems like a hollow cube. Its tension resistance in y-direction is greater than the ones in other directions, and moreover the shear tensors in three directions are weak, especially 0.0056 in z-direction.

In case 2, macrostructural topology is similar to the deterministic one, in addition to the bottom support components. Microstructural topology and periodic arrangements are similar to the corresponding deterministic ones, but their elastic tensors in the equivalent properties are slightly different. In case 3, more components appear at the bottom of the macrostructure to enhance the horizontal resistance, and four corners are connected by diagonal cross components, and the upper of the macrostructure evolves to a flat plate without holes. Microstructure seems to like a diamond-shaped structure with tensile resistance in x- and z-directions 0.1189 and 0.1100, respectively, which are about 1/3 of that in y-direction. The coupling force in xz-direction is 0.1022, larger than 0.0192 and 0.0197 in the previous two conditions. The shear resistances in both xz- and xy-directions are enhanced, while the one in yz-direction remains unchanged.

As illustrated in Fig. 10, iteration curves related to the objective function and volume fraction are smooth, which denotes topological evolutions at two scales are steadily, and the optimal designs are obtained within 94 steps. Hence, the proposed algorithm is efficient and stable to implement the concurrent design of 3D structure and material microstructure.

As illustrated in Table 9, maximum compliance, mean compliance and CV values under robust conditions are smaller than the corresponding deterministic ones, which demonstrates that robust designs are better than the corresponding deterministic ones. To visualize the 3D designs obtained in Table 8, this study simulates their printing processes in HORI software to ensure manufacturing accuracy. The printer and consumables selected are HORI z300 and 1.75MM PLA 3D FILAMENT, respectively, melting temperature is set to 200°C, the topological designs are prototyped by the fused deposition technique, as shown in Fig. 11. It is noted that experimental testing and validation for the topologically optimized and additively manufactured specimens are important in engineering practice, but these are not the major focus of this paper.

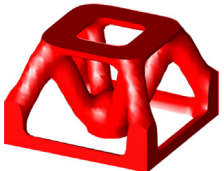
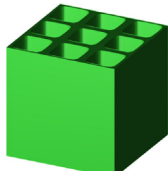
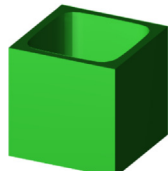

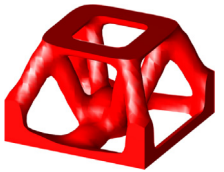
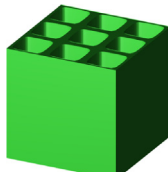
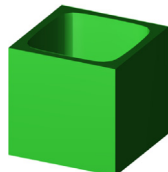





6. Conclusions

This study proposed a novel robust topology optimization method to perform the concurrent design of structures and mate-

Table 7
Parameter settings of 3D Michell-type structure.

Uncertainty type	p	θ	E	ν
Case 1	2	-90°	1	0.3
Case 2	[1.6, 2.4]	[-105°, -75°]	$N(1, 0.092)$	$N(0.3, 0.052)$
Case 3	[1.7, 2.3]	[-120°, -60°]	$N(1, 0.122)$	$N(0.3, 0.032)$

Table 8
Topological solutions and equivalent elastic properties for 3D Michell structure.

Macrostructure	Periodic arrangements	Microstructure	Half microstructure
<p>Case 1</p>  $\begin{bmatrix} 0.1876 & 0.0620 & 0.0192 & 0 & 0 & 0 \\ 0.0620 & 0.3381 & 0.0648 & 0 & 0 & 0 \\ 0.0192 & 0.0648 & 0.1968 & 0 & 0 & 0 \\ 0 & 0 & 0 & 0.0665 & 0 & 0 \\ 0 & 0 & 0 & 0 & 0.0699 & 0 \\ 0 & 0 & 0 & 0 & 0 & 0.0056 \end{bmatrix}$			
<p>Case 2</p>  $\begin{bmatrix} 0.1943 & 0.0648 & 0.0197 & 0 & 0 & 0 \\ 0.0648 & 0.3400 & 0.0638 & 0 & 0 & 0 \\ 0.0197 & 0.0638 & 0.1911 & 0 & 0 & 0 \\ 0 & 0 & 0 & 0.0687 & 0 & 0 \\ 0 & 0 & 0 & 0 & 0.0676 & 0 \\ 0 & 0 & 0 & 0 & 0 & 0.0058 \end{bmatrix}$			
<p>Case 3</p>  $\begin{bmatrix} 0.1189 & 0.0670 & 0.1022 & 0 & 0 & 0 \\ 0.0670 & 0.3409 & 0.0643 & 0 & 0 & 0 \\ 0.1022 & 0.0643 & 0.1100 & 0 & 0 & 0 \\ 0 & 0 & 0 & 0.0702 & 0 & 0 \\ 0 & 0 & 0 & 0 & 0.0680 & 0 \\ 0 & 0 & 0 & 0 & 0 & 0.0868 \end{bmatrix}$			

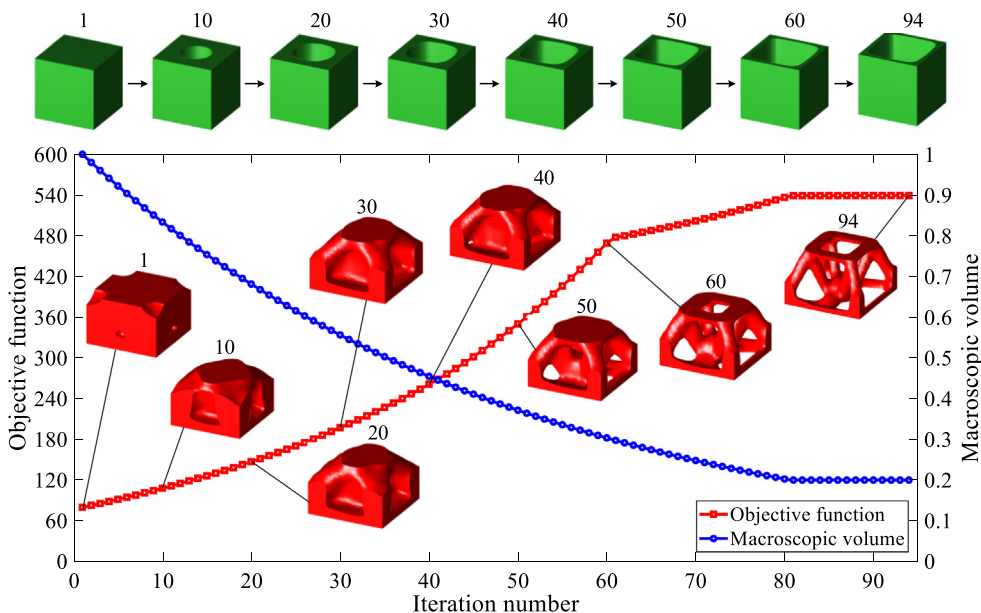


Fig. 10. Iteration histories of case 2.

Table 9
Numerical results for 3D Michell structure.

Analysis cases	Deterministic condition			Robust condition		
	Maximum compliance	Mean compliance	CV	Maximum compliance	Mean compliance	CV
Case 2	1163.4967	537.3160	0.4510	956.0238	493.8300	0.3600
Case 3	2297.2178	792.6058	0.6784	1072.1839	469.9200	0.4465

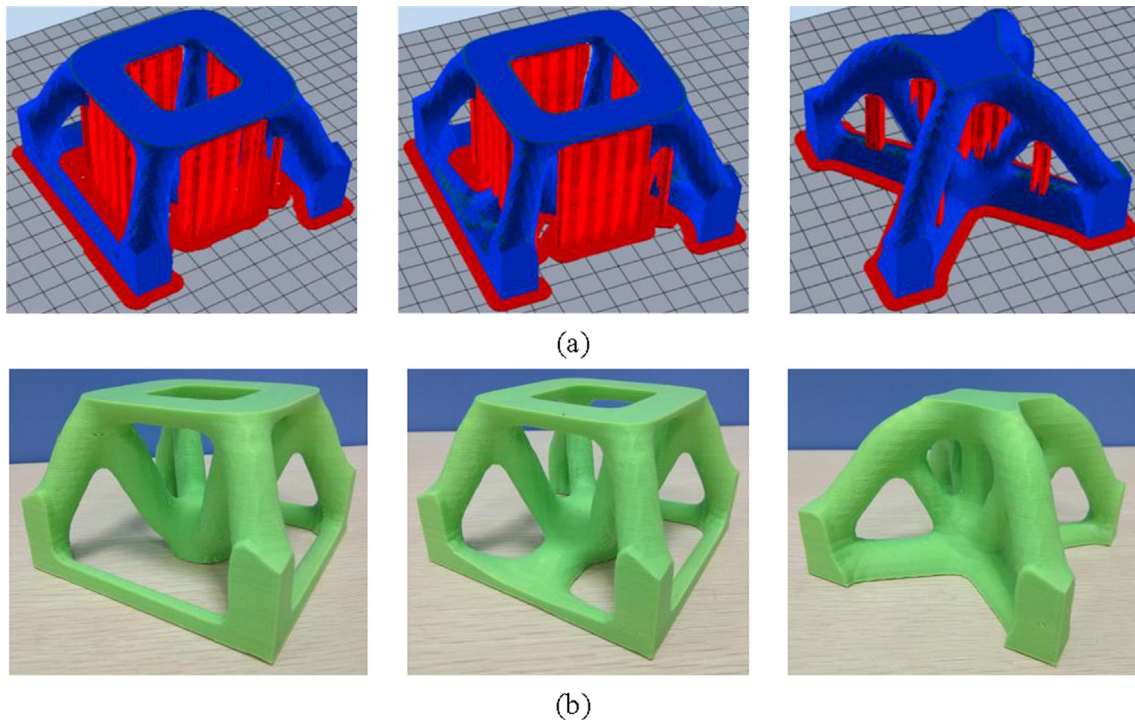


Fig. 11. 3D printing simulation and prototypes. (a) 3D printing simulation; (2) prototypes.

rial microstructures, under hybrid uncertainties in both loads and base material properties. In terms of load uncertainties described by unknown-but-bounded variables, an efficient ODUS method is proposed to avoid the time-consuming nested double loop and overestimation in most conventional methods. In terms of material uncertainties subjected to Gaussian distribution, a NIPCE method is introduced to calculate the robust objective function and two-scale sensitivities, acting as a black box without involving the original topology optimization framework. Thus, the robust objective function and two-scale sensitivities can be solved, with the help of the ODUS and NIPCE methods. Smooth BETO method are proven to be efficient to perform concurrent topology optimization. The efficiency of the proposed RTO method has been demonstrated by several 2D and 3D examples. The following conclusions can be drawn:

- (1) For the concurrent design problems with single load, the magnitude uncertainty does not affect their topological configurations, but will worsen the numerical solutions, while the directional uncertainty affects both the topological and numerical solutions.
- (2) For the concurrent design problems with multiple loads, the symmetry of the magnitude uncertainty and directional uncertainty has great influence on the topological and numerical solutions. However, the symmetrical directional uncertainty exhibits the same topologies but different numerical solutions, compared to the asymmetry of the directional uncertainty.

- (3) Material uncertainties do not affect the topological solutions of the structure and material microstructures, but have limited influence on their numerical solutions. Hence, material uncertainties in concurrent designs is dependent on the practical problems. For those with high demand of robustness, material uncertainties cannot be ignored.

Although this study investigates the concurrent designs with one type of identical microstructures, the proposed methodology and the above conclusions are applicable to the problems with multiple microstructures in robust topology optimization of structures and material microstructures.

Declaration of Competing Interest

The authors declare that they have no known competing financial interests or personal relationships that could have appeared to influence the work reported in this paper.

Acknowledgements

This research is partially supported by the Yuesui Joint Foundation for Young Scholars (2019A1515110183), the Postdoctoral Research Foundation of China (2020M682699), and the National Natural Science Foundation of China (51705158), as well as the Australian Research Council (ARC) - Discovery Projects (DP210101353).

References

- [1] E. Andreassen, J.S. Jensen, Topology optimization of periodic microstructures for enhanced dynamic properties of viscoelastic composite materials, *Struct. Multidisciplinary Optimizat.* 49 (2014) 695–705.
- [2] O. Sigmund, Tailoring materials with prescribed elastic properties, *Mech. Mater.* 20 (1995) 351–368.
- [3] O. Sigmund, Design of multiphysics actuators using topology optimization – Part I: One-material structures, *Comput. Methods Appl. Mech. Eng.* 190 (2001) 6577–6604.
- [4] J.D. Deaton, R.V. Grandhi, A survey of structural and multidisciplinary continuum topology optimization: post 2000, *Struct. Multidiscip. Optim.* 49 (2014) 1–38.
- [5] P. Liu, Y. Yan, X.P. Zhang, Y.J. Luo, Z. Kang, Topological design of microstructures using periodic material-field series-expansion and gradient-free optimization algorithm, *Mater. Des.* 199 (2020).
- [6] A.R. Diaz, O. Sigmund, A topology optimization method for design of negative permeability metamaterials, *Struct. Multidiscip. Optim.* 41 (2010) 163–177.
- [7] X.D. Huang, Y.M. Xie, Convergent and mesh-independent solutions for the bi-directional evolutionary structural optimization method, *Finite Elem. Anal. Des.* 43 (2007) 1039–1049.
- [8] G. Allaire, F. Jouve, A. Toader, Structural optimization using sensitivity analysis and a level-set method, *J. Comput. Phys.* 194 (2004) 363–393.
- [9] Z. Luo, M.Y. Wang, S.Y. Wang, P. Wei, A level set-based parameterization method for structural shape and topology optimization, *Int. J. Numer. Meth. Eng.* 76 (2010) 1–26.
- [10] W.S. Zhang, J. Yuan, J. Zhang, X. Guo, A new topology optimization approach based on Moving Morphable Components (MMC) and the ersatz material model, *Struct. Multidiscip. Optim.* 53 (2016) 1243–1260.
- [11] O. Sigmund, K. Maute, Topology optimization approaches: A comparative review, *Struct. Multidisciplinary Optimizat.* 48 (2013) 1031–1055.
- [12] Y.J. Wang, H. Xu, D. Pasini, Multiscale isogeometric topology optimization for lattice materials, *Comput. Methods Appl. Mech. Eng.* 316 (2017) 568–585.
- [13] Y.J. Wang, Z.Y. Liao, M. Ye, Y. Zhang, W.H. Li, Z.H. Xia, An efficient isogeometric topology optimization using multilevel mesh, MGCG and local-update strategy, *Adv. Eng. Softw.* 139 (2020) 102733.
- [14] D.C. Da, L. Xia, G.Y. Li, X.D. Huang, Evolutionary topology optimization of continuum structures with smooth boundary representation, *Struct. Multidiscip. Optim.* 57 (2018) 2143–2159.
- [15] H. Li, Z. Luo, L. Gao, Q.H. Qin, Topology optimization for concurrent design of structures with multi-patch microstructures by level sets, *Comput. Methods Appl. Mech. Eng.* 331 (2018) 536–561.
- [16] H. Li, Z. Luo, M. Xiao, L. Gao, J. Gao, A new multiscale topology optimization method for multiphase composite structures of frequency response with level sets, *Comput. Methods Appl. Mech. Eng.* 356 (2019) 116–144.
- [17] W.J. Chen, L.Y. Tong, S.T. Liu, Concurrent topology design of structure and material using a two-scale topology optimization, *Comput. Struct.* 178 (2017) 119–128.
- [18] Y. Zhang, L. Gao, M. Xiao, Maximizing natural frequencies of inhomogeneous cellular structures by Kriging-assisted multiscale topology optimization, *Comput. Struct.* 230 (2020) 106197.
- [19] Y. Zhang, M. Xiao, X.Y. Zhang, L. Gao, Topological design of sandwich structures with graded cellular cores by multiscale optimization, *Comput. Methods Appl. Mech. Eng.* 361 (2020) 112749.
- [20] V. Hoang, P. Tran, V. Vu, H. Nguyen-Xuan, Design of lattice structures with direct multiscale topology optimization, *Compos. Struct.* 252 (2020).
- [21] J. Zheng, Z. Luo, C. Jiang, J. Gao, Robust topology optimization for concurrent design of dynamic structures under hybrid uncertainties, *Mech. Syst. Sig. Process.* 120 (2019) 540–559.
- [22] Y.F. Zheng, M. Xiao, L. Gao, H. Li, Robust topology optimization for periodic structures by combining sensitivity averaging with a semianalytical method, *Int. J. Numer. Meth. Eng.* 117 (2019) 475–497.
- [23] P.D. Dunning, H.A. Kim, G. Mullineux, Introducing Loading Uncertainty in Topology Optimization, *AIAA J.* 49 (2011) 760–768.
- [24] K. Nabaki, J.H. Shen, X.D. Huang, Evolutionary topology optimization of continuum structures considering fatigue failure, *Mater. Des.* 166 (2019) 107586.
- [25] J.L. Wu, J. Gao, Z. Luo, T. Brown, Robust topology optimization for structures under interval uncertainty, *Adv. Eng. Softw.* 99 (2016) 36–48.
- [26] B.S. Liu, C. Jiang, G.Y. Li, X.D. Huang, Topology optimization of structures considering local material uncertainties in additive manufacturing, *Comput. Methods Appl. Mech. Eng.* 360 (2020) 112786.
- [27] H. Beyer, B. Sendhoff, Robust optimization – A comprehensive survey, *Comput. Methods Appl. Mech. Eng.* 196 (2001) 3190–3218.
- [28] J.P. Zhao, C.J. Wang, Robust topology optimization under loading uncertainty based on linear elastic theory and orthogonal diagonalization of symmetric matrices, *Comput. Methods Appl. Mech. Eng.* 273 (2014) 204–218.
- [29] Z. Kang, C.L. Wu, Y.J. Luo, M. Li, Robust topology optimization of multi-material structures considering uncertain graded interface, *Compos. Struct.* 208 (2018).
- [30] V. Keshavarzadeh, F. Fernandez, D.A. Tortorelli, Topology optimization under uncertainty via non-intrusive polynomial chaos expansion, *Comput. Methods Appl. Mech. Eng.* 318 (2017) 120–147.
- [31] V. Keshavarzadeh, K.A. James, Robust multiphase topology optimization accounting for manufacturing uncertainty via stochastic collocation, *Struct. Multidiscip. Optim.* 60 (2019) 2461–2476.
- [32] Z.C. He, H.X. Jiang, Y. Wu, E. Li, B. Zhou, Q. Tang, Robust topological design of actuator-coupled structures with hybrid uncertainties, *Acta Mech.* 1–18 (2020).
- [33] Y.F. Zheng, Y.J. Wang, X. Lu, J. Zheng, J.P. Qu, Topology optimisation for isotropic mechanical metamaterials considering material uncertainties, *Mech. Mater.* 103742 (2021).
- [34] X. Guo, X.F. Zhao, W.S. Zhang, J. Yan, G.M. Sun, Multi-scale robust design and optimization considering load uncertainties, *Comput. Methods Appl. Mech. Eng.* 283 (2015) 994–1009.
- [35] L. Wang, D.L. Liu, Y.W. Yang, J.X. Hu, Novel methodology of Non-probabilistic Reliability-based Topology Optimization (NRBTO) for multi-material layout design via interval and convex mixed uncertainties, *Comput. Methods Appl. Mech. Eng.* 346 (2019) 550–573.
- [36] Y. Wu, E. Li, Z.C. He, X.Y. Lin, H.X. Jiang, Robust concurrent topology optimization of structure and its composite material considering uncertainty with imprecise probability, *Comput. Methods Appl. Mech. Eng.* 364 (2020) 112927.
- [37] Y.F. Zheng, D.C. Da, H. Li, M. Xiao, L. Gao, Robust topology optimization for multi-material structures under interval uncertainty, *Appl. Math. Model.* 78 (2020) 627–647.
- [38] E. Andreassen, C.S. Andreasen, How to determine composite material properties using numerical homogenization, *Comput. Mater. Sci.* 83 (2014) 488–495.
- [39] Y.J. Wang, S. Arabnejad, M. Tanzer, D. Pasini, Hip Implant Design With Three-Dimensional Porous Architecture of Optimized Graded Density, *J. Mech. Des.* 140 (2018) 111406.
- [40] J.L. Wu, Z. Luo, H. Li, N. Zhang, Level-set topology optimization for mechanical metamaterials under hybrid uncertainties, *Comput. Methods Appl. Mech. Eng.* 319 (2017) 414–441.
- [41] M. Tootkaboni, A. Asadpoure, J.K. Guest, Topology optimization of continuum structures under uncertainty – A Polynomial Chaos approach, *Comput. Methods Appl. Mech. Eng.* 201 (2012) 263–275.
- [42] H. Li, L. Gao, H. Li, H.F. Tong, Spatial-varying multi-phase infill design using density-based topology optimization, *Comput. Methods Appl. Mech. Eng.* 372 (2020) 113354.
- [43] Y.F. Zheng, Y.J. Wang, X. Lu, Z.Y. Liao, J.P. Qu, Evolutionary Topology Optimization for Mechanical Metamaterials with Auxetic Property, *Int. J. Mech. Sci.* 179 (2020) 105638.
- [44] S. Das, A. Sutradhar, Multi-physics topology optimization of functionally graded controllable porous structures: Application to heat dissipating problems, *Mater. Design* (2020) 108775.
- [45] L. Xia, Q. Xia, X.D. Huang, Y.M. Xie, Bi-directional Evolutionary Structural Optimization on Advanced Structures and Materials: A Comprehensive Review, *Arch. Computat. Methods Eng.* 25 (2018) 437–478.
- [46] L. Xia, P. Breitkopf, Design of materials using topology optimization and energy-based homogenization approach in Matlab, *Struct Multidisc Optim* 52 (2015) 1229–1241.
- [47] J. Liu, G.L. Wen, Q.X. Qing, Y.M. Xie, An Efficient Method for Topology Optimization of Continuum Structures in the Presence of Uncertainty in Loading Direction, *Int. J. Comp. Meth.* 14 (5) (2017) 1750054.